The Morphology of Collisionless Galactic Rings Exterior to Evolving Bars

Micaela Bagley, Ivan Minchev, & Alice C. Quillen
Department of Physics and Astronomy, University of Rochester, Rochester, NY 14627

13 August 2008

ABSTRACT

The morphology of the outer rings of early-type spiral galaxies is compared to integrations of massless collisionless particles initially in nearly circular orbits. Particles are perturbed by a quadrupolar gravitational potential corresponding to a growing and secularly evolving bar. We find that outer rings with R1R2 morphology and pseudorings are exhibited by the simulations even though they lack gaseous dissipation. Simulations with stronger bars form pseudorings earlier and more quickly than those with weaker bars. We find that the R1 ring, perpendicular to the bar, is fragile and dissolves after a few bar rotation periods if the bar pattern speed increases by more than $\sim 8\%$, bar strength increases (by $\gtrsim 140\%$) after bar growth, or the bar is too strong ($Q_T > 0.3$). If the bar slows down after formation, pseudoring morphology persists and the R2 ring perpendicular to the bar is populated due to resonance capture. The R2 ring remains misaligned with the bar and increases in ellipticity as the bar slows down. The R2 ring becomes scalloped and does not resemble any ringed galaxies if the bar slows down more than 3.5% suggesting that bars decrease in strength before they slow down this much. We compare the morphology of our simulations to B-band images of 9 ringed galaxies from the Ohio State University Bright Spiral Galaxy Survey, and we find a reasonable match in morphologies to R1R2' pseudorings seen within a few bar rotation periods of bar formation. Some of the features previously interpreted in terms of dissipative models may be due to transient structure associated with recent bar growth and evolution.

1 INTRODUCTION

Rings in barred galaxies can exist interior to the bar, encircling the bar or exterior to the bar. For a review on classification and properties of ringed galaxies see Buta & Combes (1996). The outer rings of barred galaxies are classified as R1 or R2 depending upon whether the ring is oriented with major axis perpendicular to the bar (R1) or parallel to it (R2) (e.g., Romero-Gomez et al. 2006). If the ring is broken, partial or is a tightly wrapped spiral it is called a pseudoring and denoted R1' or R2'. Some galaxies contain both types of rings and are denoted R1R2' or R1R2. R1' and R2' morphologies were predicted as morphological patterns that would be expected near the outer Lindblad resonance (OLR) with the bar (Schwarz 1981, 1984). Rings are often the site of active star formation and so are prominent in blue visible band images, Hα narrow band images, and HI emission (Buta & Combes 1996).

Orbital resonances, denoted Lindblad Resonances, occur at locations in the disk where

$$\Omega_b = \Omega \pm \kappa/m \qquad (1)$$

where Ω_b is the angular rotation rate of the bar pattern and m is an integer. Here $\Omega(r)$ is the angular rotation rate of a star in a circular orbit at radius r and $\kappa(r)$ is the epicyclic frequency. The $m = 2$ OLR is that with $\Omega_b = \Omega + \kappa/2$. Orbits

of stars are often classified in terms of nearby periodic orbits that are closed in the frame rotating with the bar. Near resonances orbits become more elongated and have higher epicyclic amplitudes. Exterior to the OLR periodic orbits parallel to the bar are present whereas interior to the OLR both perpendicular and parallel periodic orbits are present. For a steady pattern, closed orbits interior to the OLR are expected to be aligned with major axis perpendicular to the bar whereas those exterior to the OLR are aligned parallel to it (e.g., Contopoulos & Grosbol 1989; Kalnajs 1991).

A common assumption is that rings form because gas accumulates at resonances. This follows as gas clouds cannot follow self-intersecting orbits without colliding. Because of dissipation in the gas, the bar can exert a net torque on the gas leading to a transfer of angular momentum. The torque is expected to change sign at resonances so gas can move away from them or accumulate at them. The CR region is expected to be depopulated leading to gas concentrations at the OLR and ILR resonances. Gaseous rings form when gas collects into the largest periodic orbit near a resonance that does not cross another periodic orbit (Schwarz 1984).

Schwarz (1981, 1984) first demonstrated the efficiency of this process. Other papers have confirmed and extended this work (e.g., Combes & Gerin 1985; Byrd et al. 1994; Salo et al. 1999; Rautiainen & Salo 2000; Rautiainen et al.

2004). Because dissipation is thought to be important, spiral like features and ovals that are not perfectly aligned with the bar, similar to those observed, are predicted. In some cases galaxy morphology and kinematics have not been successfully modeled with a single steady state bar component. Improvements in the models have been made with the addition of an additional exterior oval or spiral component (e.g., Hunter et al. 1988; Lindblad et al. 1996).

Previous work accounting for ring galaxy morphology has primarily simulated the gas dynamics using sticky particle simulations that incorporate dissipative or inelastic collisions. Rautiainen & Salo (2000) ran N-body stellar simulations coupled with sticky gas particles. These simulations have self-consistent bars so that the orbits of the stars in the bars are consistent with the bar's gravitational potential. The disadvantage of using N-body simulations is that the properties of the bar such as its pattern speed and strength cannot be set. They can only be changed indirectly by varying the initial conditions of the simulations. An alternative approach is to set the bar perturbation strength, shape and pattern speed and search for likely bar parameters consistent with the properties of observed galaxies (e.g., Salo et al. 1999; Rautiainen et al. 2004, 2008).

Previous work has explored the affect of bar strength and pattern speed on ring morphology (e.g., Salo et al. 1999; Rautiainen et al. 2004, 2008) and length of time since the bar grew (e.g., Rautiainen & Salo 2000; Ann & Lee 2000). Here we explore the role of bar evolution on ring galaxy morphology. By bar evolution we mean changes in bar pattern speed and strength during and after bar growth. N-body simulations lacking live halos predict long lived bars with nearly constant pattern speeds (e.g., Voglis et al. 2007). However angular momentum transfer between a bar and the gas disk either interior or exterior to the bar or between a bar and a live halo can cause the pattern speed to vary (e.g., Debattista & Sellwood 1998; Bournaud & Combes 2002; Das et al. 2003; Athanassoula 2003; Sellwood & Debattista 2006; Martinez-Valpuesta et al. 2006). Thus constraints on the secular evolution of bars could tell us about the coupling between bars, gas and dark halos.

Gas and stars exterior to a bar are sufficiently distant and moving sufficiently slowly compared to the bar that they are unlikely to cause strong perturbations on the orbits of stars in the bar. Because a calculation of the gravitational potential involves a convolution with an inverse square law function, high order Fourier components are felt only extremely weakly exterior to the bar. The dominant potential term exterior to the bar is the quadrupolar term which decreases with radius to the third power, $\Phi \propto r^{-3}$.

Here we explore the role of a changing quadrupolar potential field on the morphology of stars exterior to a bar. In this work we focus on collisionless stellar orbits and leave investigating the study of dissipative effects for future study. In Section 2 we describe our simulations and present the results obtained by varying the parameters. In Section 3 we compare the results of our simulations with 9 galaxies from the Ohio State University Bright Spiral Galaxy Survey (Eskridge et al. (2000), hereafter OSUBSGS). Finally in Section 4 we summarize and discuss our results.

2 TEST PARTICLE SIMULATIONS

We perform 2D test-particle simulations of an initially axisymmetric galactic disk that is perturbed by a forcing bar pattern. The rotation curve adopted for a particle in a circular orbit is

$$v_c(r) = s^{\gamma/2} \tag{2}$$

with $s = \sqrt{r^2 + a^2}$ and $a > 0$ a core radius to prevent extreme orbits near the galaxy center. A flat rotation curve has $\gamma = 0$. This curve corresponds to an axisymmetric potential

$$\Phi_0(s) = \begin{cases} \log(s) & \text{for } \gamma = 0 \\ \gamma^{-1} s^\gamma & \text{for } \gamma \neq 0 \end{cases} \tag{3}$$

To this axisymmetric component we add a quadrupole perturbation for the bar in the form used by Dehnen (2000); Minchev et al. (2007),

$$\Phi_b(r, \phi, t) = \epsilon \cos\left[2(\phi - \Omega_b t)\right] \times \begin{cases} (r_b/r)^3, & r > r_b, \\ 2 - (r/r_b)^3, & r \leqslant r_b. \end{cases} \tag{4}$$

where r_b is the bar length and Ω_b its angular rotation rate or pattern speed.

As we wish to explore bars with changing pattern speeds we allow Ω_b to vary with time; however, we fix the ratio of the bar length to the corotation radius, R, so that

$$r_b(t) = r_{b,0} \frac{\Omega_{b,0}}{\Omega_b(t)}. \tag{5}$$

Previous studies have found that bars end interior to their corotation radius, r_{CR}, with the ratio of bar length to bar corotation radius $R = 0.7 - 0.9$ (Athanassoula 1992; Rautiainen et al. 2008). We describe pattern speed variations with two parameters: the rate of change during bar growth, $d\Omega_g/dt$, and that after bar growth, $d\Omega_b/dt$. The bar strength grows linearly with time, $\epsilon \propto t$, until a time t_{grow}, at which time it reaches a strength ϵ_{tgrow}. After t_{grow} the bar strength may vary at a slower rate, $d\epsilon/dt$.

Previous work has used as a measure of bar strength the parameter Q_T (Combes & Sanders 1981). At a given radius this is the ratio of the maximum tangential force to the azimuthally averaged radial force. Here equation (4) implies that the maximum value of Q_T is $Q_T = 2\epsilon/v_c^2$.

The simulations presented here integrate 10^5 particles with a 4th order Runge-Kutta method. All particles are integrated simultaneously in parallel on a NVIDIA GeForce 8800 GTX graphics card. The code is written with NVIDIA's CUDA (Compute Unified Device Architecture), the C-language development environment for CUDA enabled Graphics Processing Units (GPUs).

Particle initial conditions are nearly circular orbits with epicyclic amplitude randomly generated so the initial velocity dispersion is σ times the circular velocity. In our simulations the velocity dispersion is about 0.04 of the circular velocity, which is about 7 km/s for a galaxy with a 200 km/s rotational velocity. For comparison, HI line widths are typically in the range of 5-10 km/s. The epicyclic amplitude distribution is Gaussian. Initial radii are chosen from a flat distribution with minimum and maximum radius between 0.5 and 4.0 times the initial bar length. This leads to an initial disk surface density proportional to $1/r$.

Unless otherwise noted, when we discuss times in terms of bar periods we are referring to the initial bar period,

which has time $P_{b,0} = 2\pi/\Omega_{b,0}$. We run our simulations for twenty-five bar periods, and the bar grows for the first three bar rotation periods; $t_{grow} = 3$. We focus on a ratio of bar length to corotation radius of $R = 0.8$, so that the initial bar pattern speed is $\Omega_{b,0} = 0.8$ and the corotation radius is therefore $r_{CR} = 1.25$. Table 1 lists the initial conditions that all of our simulations have in common. Table 2 lists remaining simulation parameters. The majority of our simulations have bars of strength $|\epsilon_{tgrow}| = 0.10$, corresponding to $Q_T = 0.2$. Lengths are given in terms of the initial bar length, $r_{b,0}$, and angular velocities are given in terms of that at a radius of the initial bar length. We use negative values of ϵ to signify that the bar is initially oriented horizontally.

2.1 Description of simulations

Snapshots at different times for simulation 1 with parameters listed in Tables 1 and 2 are shown in Figures 1 and 2. Simulation 1 is our base or comparison simulation, with $|\epsilon_{tgrow}| = 0.10$, corresponding to $Q_T = 0.2$, and bar grown in $t_{grow} = 3$ bar rotation periods. In Figures 1 and 2 each frame has been rotated so that the bar is horizontal. Figure 1 shows the first 3 bar periods of bar growth of simulation 1 with each image separated in time by a quarter bar period. Figure 2 shows snapshots of the 25 bar periods of the simulation with each image separated by a full bar period. As can be seen from Figure 1, during bar growth, strong open spiral-like structure is present that might be interpreted as an R1' ring. Just after bar growth (see Figure 2), both R1 and R2 rings are present but the R2 ring is not always oriented parallel to the bar. For up to 5 bar rotation periods following bar growth, there are azimuthal variations in density in the rings as well as shifts in the R2 ring orientation so they could be considered pseudorings. After bar growth the structure stabilizes and R1 and R2 rings remain that are increasingly mirror symmetric and remain oriented perpendicular and parallel to the bar, respectively.

The bar is grown sufficiently slowly that the orbits change adiabatically. Orbits remain near to closed or periodic orbits and structure associated with both R1 and R2 orbit families is seen. Most interesting is that the simulation displays twists in the density peaks, azimuthal variations in the density of the ring and deviations of ring orientation from perpendicular and parallel to the bar at the end of and a few periods after bar growth. Previous work has suggested that weak dissipation is required to exhibit spiral structure or pseudoring morphology, however here we see transient spiral structures induced by bar growth and pseudoring type morphology for a few rotation periods following bar growth. After ~ 5 periods the asymmetries are reduced and the morphology contains both stable R1 and R2 type rings.

Our simulation looks similar to the sticky particle simulations by Schwarz (1981); Byrd et al. (1994). Their simulations also displayed early spiral structure. The sticky particle simulations exhibit strong R1' morphology for a few bar rotation periods. Our simulation exhibits R1' type morphology only during bar growth, R1R2' morphology a few rotation periods after bar growth and stable R1R2 morphology on long timescales.

During bar growth these simulations look remarkably similar to the sticky particle simulations by Rautiainen et
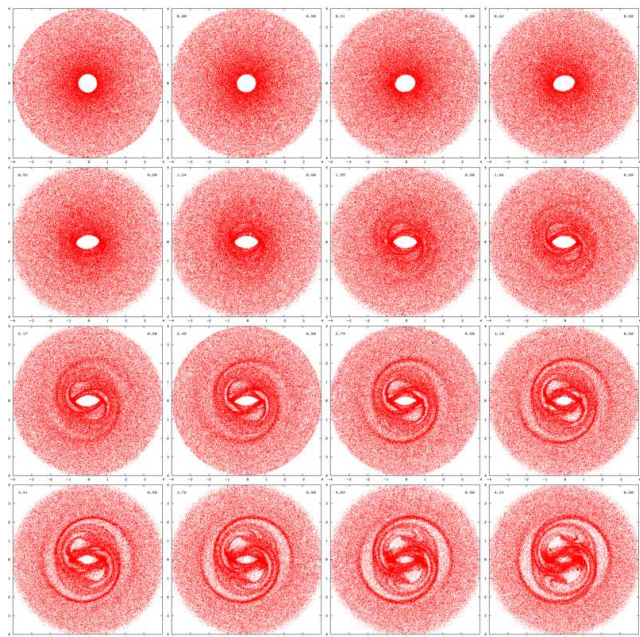

Figure 1. Bar growth in simulation 1. The distribution of collisionless particles is shown every quarter bar period. The bar is growing up to the left frame of the last row. Strong open spiral-like structure is evident during bar growth even though the simulation is lacking gaseous dissipation.

al. (2004, 2008) even though they lack dissipation. N-body and SPH simulations often suffer from artificially heating. Fine structure that would only be present in a perturbed initially cold population might not survive due to excess heating inherent in the simulation. Sticky particle and SPH simulations, because they allow dissipation, can reduce the velocity dispersion of the particles. The similarity between the sticky particle simulations and the dissipationless simulations shown here could be because our initial orbits were nearly circular.

The ability of collisionless simulations to display R1R2 type morphology suggests that we reexamine the role of dissipation in influencing ring galaxy morphology. SPH simulations (Ann & Lee 2000; Bissantz et al. 2003) sometimes show open outer spiral arms that are similar to R1' pseudorings and resemble morphology during bar growth seen here. However our simulations stop showing spiral structure soon after bar growth. The SPH simulations by Ann & Lee (2000) show R1' type pseudoring morphology but only within a few rotation periods after bar growth. Likewise the sticky particle simulations by Rautiainen & Salo (2000) show R1 or R2 or both R1R2 ring morphology, but only within a few bar rotation periods after bar growth (see their figure 10). The SPH simulations by Ann & Lee (2000) show spiral structure for a somewhat longer time than ours (a few bar rotations following bar growth) but they fail to exhibit R1 or R2 ring morphology.

We find that R1R2 rings (systems with both types of features) do not require dissipation for formation, however they do require particles to be on nearly closed orbits. This can result either because of dissipation or because gas and recently born stars tend to be on nearly circular orbits prior to bar growth. The success of sticky particle simulations in
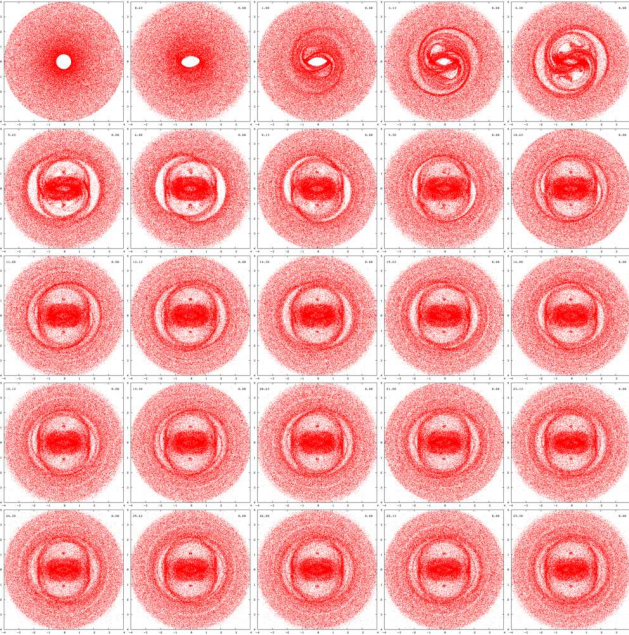
Figure 2. Simulation 1, with bar angular rotation rate $\Omega_{b,0} = 0.8$, bar strength $|\epsilon_{tgrow}| = 0.10$ (corresponding to $Q_T = 0.2$) and bar grown in $t_{grow} = 3$ bar periods. The distribution of collisionless particles is shown each full bar rotation period, and the entire 25 bar periods of the simulation are shown. The bar is growing up to the fourth frame. We note that the R2 ring is misaligned with bar and azimuthal variations in densities are seen until $\sim t = 5$ bar rotation periods after bar formation. Pseudoring morphology is present at the end of and a few rotation periods after bar growth. Both R1 and R2 rings are present and stable after bar growth. We find that collisionless particles that are initially in nearly circular orbits can display R1R2 outer ring morphology.

reproducing outer ring morphology, may be in part because of their ability to cool or reduce the velocity dispersion of their particles. SPH simulations (e.g., Ann & Lee 2000; Bissantz et al. 2003) exhibit only R1' pseudoring morphology suggesting that when dissipation is large, both types of rings are not formed. Recent SPH and sticky particle simulations fail to exhibit long lived R1R2 morphology. Here however we see that R1R2 morphology can be long lived, though it's possible that R1R2 ring morphology is a short lived phenomenon as many barred galaxies do not exhibit R1 or R2 type outer rings.

2.2 Morphology sensitivity to pattern speed variation after bar growth

We first explore the sensitivity of outer ring morphology to weak changes in bar pattern speed following bar growth. Simulations 2-6 are identical to simulation 1 except the bar pattern speed increases after bar growth. Simulations 7-11 are identical to simulation 1 except the bar pattern speed decreases after bar growth. Figure 3 shows simulation 5 that has an increasing bar pattern speed $d\Omega/dt = 0.0004$. For this simulation the pattern speed increases 0.39% each bar period. We find that the R1 outer ring grows weaker as the pattern speed increases. The R1 completely dissolved by the end of the simulation when the pattern speed has increased by about 9% compared to its initial value. At later
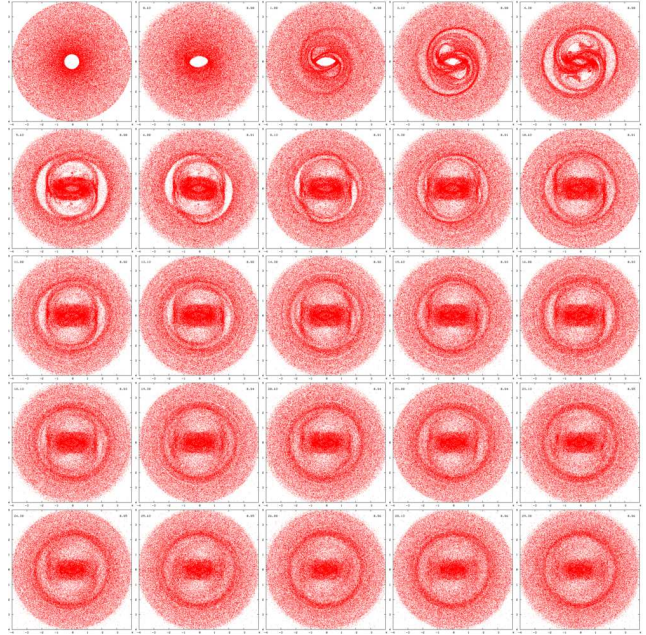

Figure 3. Simulation 5 showing a bar with increasing pattern speed, $d\Omega_b/dt = 0.0004$. The bar speeds up only after it has finished growing at 3 bar rotation periods. Each frame is separated by one full initial bar rotation period. Note the loss of the R1 ring later in the simulation.

times, even though the perturbation is always changing the morphology is nearly mirror symmetric. We find that spiral structure or pseudoring structure is not caused by the increase in bar pattern speed.

Figure 4 shows the morphology at the end of simulations 1-6. Here we see that the R1 ring disappears as the bar pattern speed increases. At later times in the simulations with more quickly increasing pattern speeds the R1 ring dissolves and only a nearly circular outer ring remains. We find that when the bar pattern speed increases by more than $\sim 8\%$, the R1 ring completely dissolves.

In simulations 7-11 we decrease the bar pattern speed after bar growth. Figure 5 shows simulation 11 with $d\Omega_b/dt = -0.0003$. The R2 ring in this simulation is elongated and strong and is seldom aligned parallel to the bar even at later times. While the simulation with the increasing pattern speed (shown in Figure 3) did not exhibit pseudoring morphology after bar growth or misaligned R1 or R2 rings, the simulations with decreasing pattern speed do show misaligned R2 type rings even at late times. The ellipticity of the R2 ring is higher than seen in the comparison simulation shown in Figure 2 with a bar with a constant pattern speed.

Figure 6 shows the last periods of simulations 1 and 7-11. Here we see that the R2 ring remains misaligned 22 bar periods after bar growth is complete when the pattern speed begins to decrease. The ellipticity of the R2 ring increases as the bar pattern speed decreases. We find that when the pattern speed decreases by more than $\sim 3.5\%$, the simulations do not resemble real galaxy morphology.

Decreasing the pattern speed moves the bar's resonances outwards. Exterior to the OLR only one family of periodic orbits exits aligned parallel to the bar. However interior to the bar, two families of periodic orbits exist, both
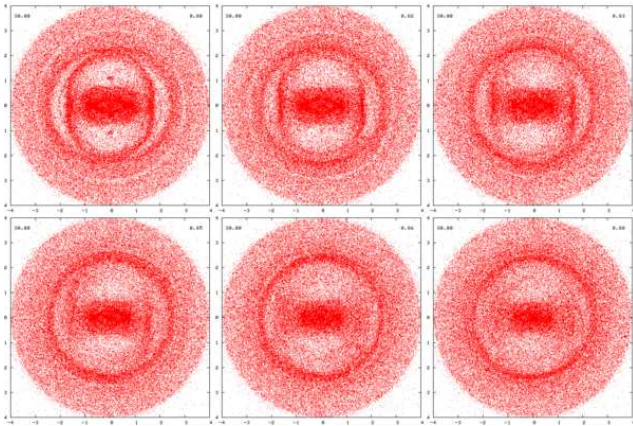
Figure 4. The last frame of simulations 1-6. Each frame shows the density distribution at a time 25 bar periods after the start of the simulation. From left to right the top row shows simulation 1 with $d\Omega_b/dt = 0.0$; simulation 2 with $d\Omega_b/dt = 0.0001$ and simulation 3 with $d\Omega_b/dt = 0.0002$. The bottom row shows simulation 4 with $d\Omega_b/dt = 0.0003$; simulation 5 with $d\Omega_b/dt = 0.0004$ and simulation 6 with $d\Omega_b/dt = 0.0005$. We find that when the bar pattern speed increases by more than $\sim 8\%$ the R1 ring completely dissolves.
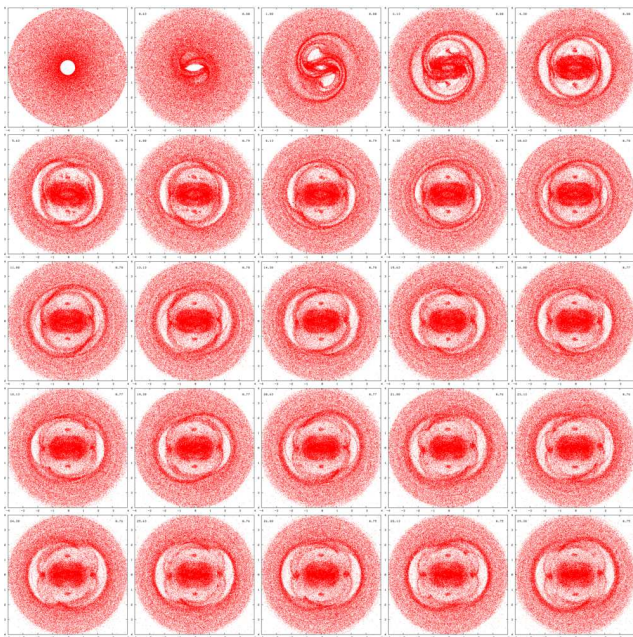

Figure 6. The last frame of simulations 1 and 7-11. Each frame shows the density distribution at a time 25 bar periods after the start of the simulation. From left to right the top row shows simulation 1 with $d\Omega_b/dt = 0.0$, simulation 7 with $d\Omega_b/dt = -0.0001$ and simulation 8 with $d\Omega_b/dt = -0.00015$. The bottom row shows simulation 9 with $d\Omega_b/dt = -0.0002$, simulation 10 with $d\Omega_b/dt = -0.00025$ and simulation 11 with $d\Omega_b/dt = -0.0003$. We attribute the high epicyclic amplitude R2 rings to resonance capture. The R2 ring remains misaligned with the bar even 22 bar periods after the bar pattern speed began decreasing.

Figure 5. Simulation 11 showing a bar with decreasing pattern speed, $d\Omega_b/dt = -0.0003$. The bar slows down after it has finished growing. Each frame is separated by one full bar rotation period. We see a high epicyclic amplitude R2 ring that we attribute to resonance capture. This ring can be misaligned with the bar even at late times.

those perpendicular and parallel to the bar (e.g., Contopoulos & Grosbol 1989; Quillen 2003). When the bar slows down orbits can be captured into resonance (e.g., Romero-Gomez et al. 2006). Only the orbit family parallel to the bar can capture particles, and as the bar pattern speed continues to decrease these orbits will increase in epicyclic amplitude. This is mathematically similar to Pluto's orbit increasing
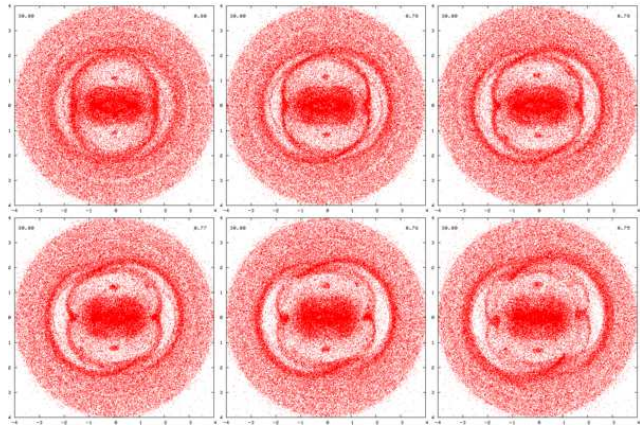
in eccentricity as Neptune migrates outwards (e.g., Quillen 2006). Resonance capture into orbits parallel with the bar is likely to explain the higher epicyclic amplitude of the R2 rings seen in Figure 5 in which the bar pattern is slowing down.

In summary if the bar speeds up subsequent to bar formation (or increases in pattern speed by more than $\sim 8\%$) we find that the R1 ring dissolves. Simulations with increasing pattern speeds show misaligned rings and azimuthal density contrasts only 1-2 periods after bar formation. If the bar slows down however, we find that the R2 ring is increased in strength and eccentricity and both R2 and R1 are seen even at later times (> 20 periods after bar formation). Furthermore the R2 ring is misaligned with the bar for many rotation periods. If the bar decreases by more than $\sim 3.5\%$ we find that the R2 becomes unrealistically scalloped.

2.3 Morphology sensitivity to pattern speed variation during bar growth

We next explore the effect of altering the bar pattern speed during bar growth rather than following bar growth. $d\Omega_g/dt$ is positive in simulations 12-15, causing the pattern speed to increase for the first 3 periods of each simulation. Figure 7 shows simulation 13 with $d\Omega_g/dt = -0.01$. Open spiral arms are present at the end of the third period of bar growth. However, R1R2 double ring morphology does not form in this simulation. As was true in the simulations with bar pattern speed increasing following bar formation (simulations 2-6; see Figures 3 and 4) the R1 ring dissolves and only a nearly circular outer ring remains. We note that the spiral and outer ring structure in simulations 2-6 (see 3) did not dissolve as quickly as in simulation 13, where an R1R2 outer ring never forms. This suggests that outer ring structures are more sensitive to alterations in pattern speed during bar growth than to changes after bar growth.
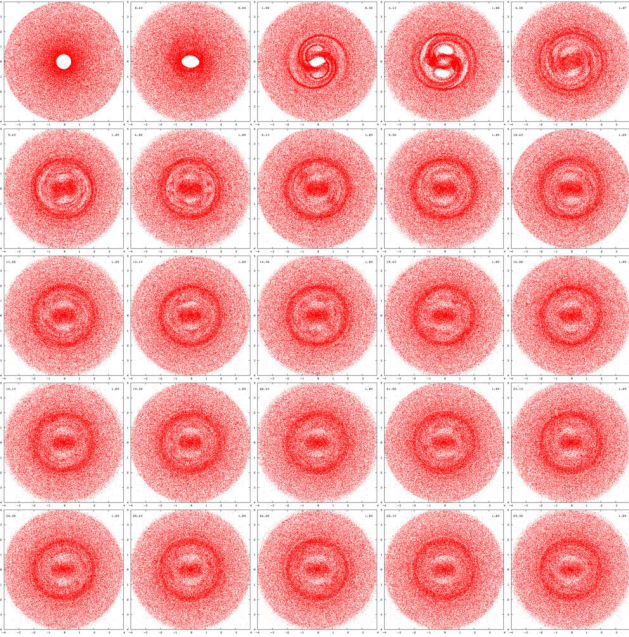
Figure 7. Simulation 13 showing a bar with increasing pattern speed during bar growth, $d\Omega_g/dt = 0.01$. The bar pattern speed is only increasing in the first three frames while the bar is growing. Each frame is separated by one full initial bar period. R1R2 structure does not form as it does in Figure 3 where the pattern speed is increasing after bar growth. Here spiral structure dissolves within 3 periods after bar growth and only a nearly circular outer ring remains. Outer ring structures may be more sensitive to alterations in pattern speed during bar growth than to changes after bar growth.

Figure 8. Morphology change when the pattern speed is increased during bar growth. Five frames, corresponding to the last 2 periods of bar growth, of the simulations in which the pattern speed is increased during growth. From top to bottom the rows show simulation 1 with $d\Omega_g/dt = 0.0$; simulation 12 with $d\Omega_g/dt = 0.005$; simulation 13 with $d\Omega_g/dt = 0.01$; simulation 14 with $d\Omega_g/dt = 0.015$ and simulation 15 with $d\Omega_g/dt = 0.02$. As the pattern speed increases, the axes of the rings decreases.

Figure 8 shows the last 2 of the 3 periods of bar growth for simulations 1 and 12-15. The first row shows simulation 1 with $d\Omega_g/dt = 0.0$. $d\Omega_g/dt$ increases by 0.005 in each consecutive simulation, corresponding to each row in Figure 8. We note from these simulations that open spiral arms are seen during bar growth when the bar is increasing in pattern speed. The radii of spiral structure decreases as the pattern speed increases. This is expected as the radii of the resonances move inward as the bar pattern speed increases.

Figure 4 shows that ring radial size does not decrease as the bar pattern speed increases when the pattern speed increases after bar growth. However when the pattern speed increases during bar growth (see Figure 8) the ring radius does decrease. This suggests that ring size is primarily set during bar growth and is not strongly affected by subsequent increases in pattern speed. Subsequent bar speed increases primarily dissolves or weakens the rings rather than changes their radius.

We now compare the effect of decreasing pattern speed during bar growth with the effect of increasing pattern speed during bar growth. The pattern speed is decreasing during the 3 periods of bar growth in simulations 16-19. Figure 9 shows the entire simulation 17 with $d\Omega_g/dt = -0.005$, while Figure 10 shows the last 2 of the 3 periods of bar growth for simulations 1 and 16-19. We find that when the bar pattern slows down during bar growth the outer rings are not lost as was true when the pattern speed increased during growth. The R1R2' structure seen during bar growth for simulation 1 is exhibited by this simulation but later, 2 to 3 periods
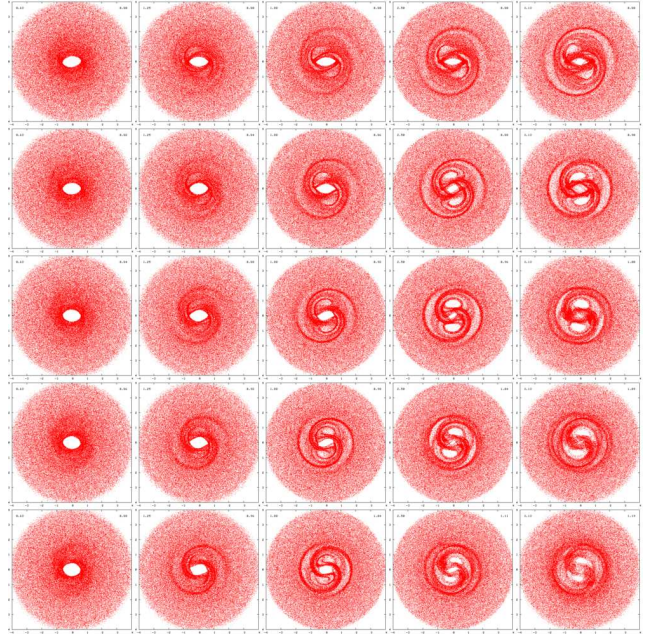
after bar growth rather than in the first period following bar growth. During this time the rings appear almost double or tightly wound. The pseudorings close, the morphology stabilizes and presents the R1R2 structure characteristic of our steady state comparison simulation shown in Figure 2. As is expected from the location of the OLR, the ring radii become larger if the bar pattern speed decreases.

The first row of Figure 10 shows simulation 1 with $d\Omega_g/dt = 0.0$. $d\Omega_g/dt$ decreases by 0.0025 in each consecutive simulation, corresponding to each row in Figure 10. The decreasing pattern speed seems to delay the formation of strong spiral structure. Figure 8 showing morphology during bar growth for a bar that is speeding up can be compared to Figure 10 that shows morphology during bar growth for a bar that is slowing down. The simulation with the largest decrease in pattern speed shows the weakest spiral structure during bar growth and that with the largest increase in pattern speed the strongest spiral structure earliest.

In summary, we find that if the bar pattern speed is decreasing during growth, transient spiral structure is weaker during growth and the formation of the R1 and R2 ring structure is delayed by a few bar rotation periods. If the bar pattern speed increases during rather than after growth, the outer rings are smaller. An increase in pattern speed during bar growth destroys the R1 ring and asymmetries typical of pseudorings.
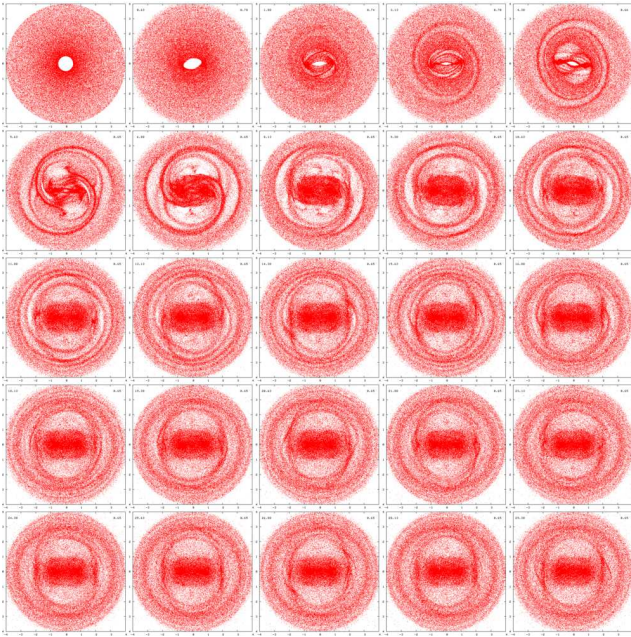
Figure 9. Simulation 17 with $d\Omega_g/dt = -0.005$. The pattern speed is decreasing during bar growth. Each frame is separated by one full bar rotation period. The transient spiral structure during bar growth is weaker than when bar pattern is fixed (see top row of Figure 2). Formation of the R1 and R2 rings is delayed in this simulation and occurs after the bar has finished growing compared to that with a fixed pattern speed.
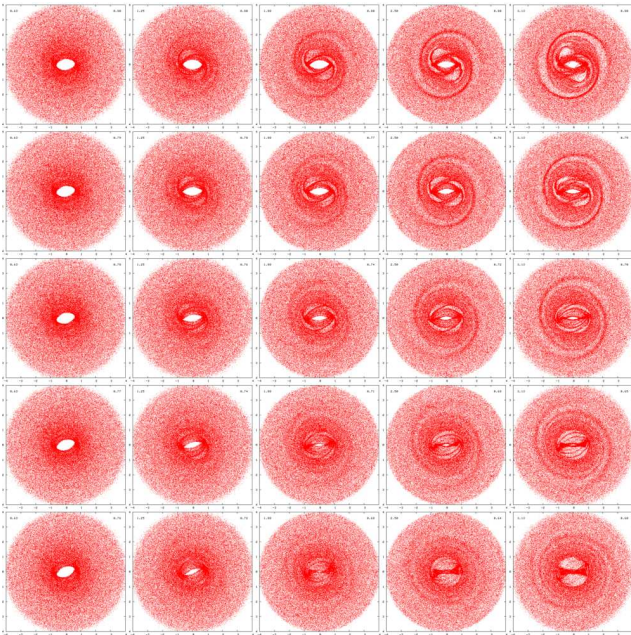

Figure 10. Morphology change when the pattern speed is decreased during bar growth. Five frames, corresponding to the last 2 periods of bar growth, of the simulations in which the pattern speed is decreased during bar growth. From top to bottom the rows show simulation 1 with $d\Omega_g/dt = 0.0$; simulation 16 with $d\Omega_g/dt = -0.0025$; simulation 17 with $d\Omega_g/dt = -0.005$; simulation 18 with $d\Omega_g/dt = -0.0075$; and simulation 19 with $d\Omega_g/dt = -0.01$. Transient spiral structure during bar growth is weaker when the bar is slowing down.
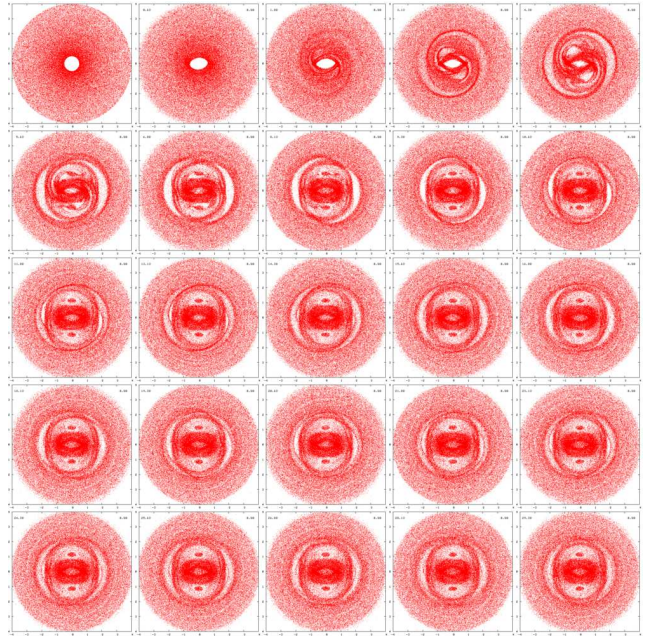
Figure 11. Simulation 21 for a weak bar with $|\epsilon_{tgrow}| = 0.08$ corresponding to $Q_T = 0.16$. This is a weaker bar than that of simulation 1 shown in Figure 2 where $|\epsilon_{tgrow}| = 0.10$. Each frame is separated by one full bar period. The R2 ring is misaligned with the bar for up to 6 bar periods after bar growth, longer than the R2 ring in Figure 2. At late times stable R1 and R2 rings form and remain mirror symmetric.

2.4 Morphology sensitivity to bar strength

We now explore the sensitivity of the morphology to bar strength. The bar strength increases linearly with time during bar growth until, at $t = t_{grow}$, it reaches a strength determined by the parameter $|\epsilon_{tgrow}|$. Thus a lower value of $|\epsilon_{tgrow}|$ results in both a weaker bar at $t = t_{grow}$ and a slower rate of bar growth. Figure 11 shows simulation 21 with $|\epsilon_{tgrow}| = 0.08$ corresponding to $Q_T = 0.16$. This is a weaker bar than that of our comparison simulation shown in Figure 2 where $|\epsilon_{tgrow}| = 0.10$. During and right after bar growth we see the open spiral structure evident in Figure 2. Here the R2 ring is misaligned with the bar for up to 6 bar rotation periods following bar growth, whereas the R2 ring in Figure 2 is misaligned for 5 bar periods following bar growth. The timescale for misalignment in the R2 ring is probably related to the bar strength, which would set the libration timescale in the OLR. The R1 and R2 rings become increasingly mirror symmetric. They remain strong, stable, and oriented perpendicular and parallel to the bar, respectively.

Figure 12 shows simulation 23 with $|\epsilon_{tgrow}| = 0.14$ corresponding to $Q_T = 0.28$. This is a stronger bar than that of our comparison simulation shown in Figure 2. The spiral structure evident during and right after bar growth is much stronger than that of either Figure 11 or Figure 2. The R2 ring is misaligned with the bar for only 3 to 4 bar periods following bar growth. R1 and R2 rings form earlier, and we see a weakening of the R1 ring at later times of the simulation.

In Figure 13 we compare the last 2 periods of bar growth of simulation 1 and simulations 20-24. $|\epsilon_{tgrow}|$ increases from 0.06 (top row of Figure 13) to 0.16 (bottom row). Strong
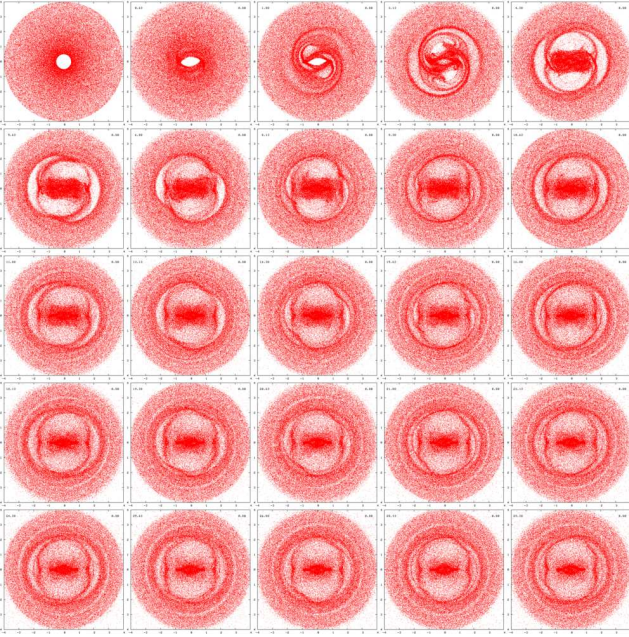
Figure 12. Simulation 23 for a strong bar with $|\epsilon_{tgrow}| = 0.14$ corresponding to $Q_T = 0.28$. This is a stronger bar than that shown in Figure 2. Each frame is separated by one full bar period. The R2 ring is only misaligned with the bar for 3 bar periods after bar growth. The R1R2 structure is evident earlier than in Figure 11 but the R1 ring weakens at the end of the simulation.

transient spiral structure forms noticeably earlier when the bar is stronger.

By the third period of simulation 24 in the bottom row, $|\epsilon_{tgrow,24}| = 0.16$ ($Q_T = 0.32$), the pseudoring structure most closely resembles that of the fourth period of simulation 1, $|\epsilon_{tgrow,1}| = 0.10$. Simulation 24 exhibits closed R1R2 structure a half period after bar growth, whereas simulation 1's R1R2 structure is not evident until 1.5 periods after bar growth. Thus, a 60% increase in bar strength accelerates pseudoring formation such that closed-orbit rings are evident one bar period earlier.

We now consider the structure at later times as a function of bar strength. Figure 14 shows the last bar period of each of the same six simulations, simulations 1 and 20-24. The bar strength, $|\epsilon_{tgrow}|$, increases by 0.02 in each successive simulation. In the first and second frames we see a very strong concentration of particles in the R1 ring. By the last frame in the second row, however, the R1 ring is almost completely gone. Thus, though the increased bar strength accelerates ring formation at early times, we find that the R1 outer ring dissolves at later times when the bar strength is high, just as it does in Figure 3 when the pattern speed is increasing after bar growth.

The concentrations of particles above and below the bar that are evident in Figure 11 and in the weaker bars shown at later times in Figure 14 are the L4 and L5 Lagrange points and so are corotating with the bar. Small changes in the orbits circulating around these points would cause the particles to circle the bar rather than remain confined to the vicinity of the L4 or L5 point corotating with the bar (e.g., Contopoulos & Patsis 2006). Small variations in pattern speed during or after bar growth (e.g., see Figures 4
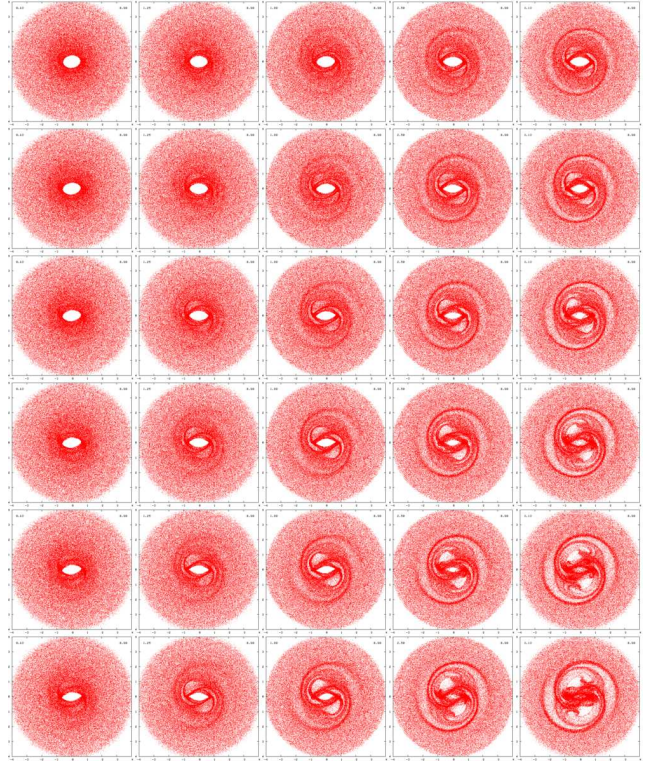

Figure 13. Morphology change when the bar strength is altered. Five frames, showing the last 2 periods of bar growth, of simulations 1 and 20-24. From top to bottom the rows show simulation 20 with $|\epsilon_{tgrow}| = 0.06$, $Q_T = 0.12$; simulation 21 with $|\epsilon_{tgrow}| = 0.08$, $Q_T = 0.16$; simulation 1 with $|\epsilon_{tgrow}| = 0.10$, $Q_T = 0.2$; simulation 22 with $|\epsilon_{tgrow}| = 0.12$, $Q_T = 0.24$; simulation 23 with $|\epsilon_{tgrow}| = 0.14$, $Q_T = 0.28$; and simulation 24 with $|\epsilon_{tgrow}| = 0.16$, $Q_T = 0.32$. By the end of the fifth frame, $t = t_{grow}$ and the strength of the bar is equal to the value of the parameter $|\epsilon_{tgrow}|$. Bars with higher values of $|\epsilon_{tgrow}|$, i.e. stronger bars that grow faster, develop strong spiral structure and outer rings earlier. By the end of the 3 periods of bar growth, our strongest bar (simulation 24, $|\epsilon_{tgrow}| = 0.16$) has pseudorings that have almost fully closed to form an R1R2 ring.

and 7) and stronger bars (e.g., Figure 14) reduce the number of particles near these points. We note that stars and gas are not commonly seen in galaxies at these points, suggesting that weak bars with unchanging pattern speeds and strengths do not persist in galaxies.

2.5 Morphology sensitivity to slow variations in bar strength after bar growth

We now consider variations in bar strength after bar growth. In simulations 25-29, we allow the bar strength to grow linearly with time after $t = t_{grow}$. Figure 15 shows simulation 26 with increasing bar strength. The bar strength at the end of bar growth is $|\epsilon_{tgrow}| = 0.10$. It then continues to increase in strength at a slower rate with $d|\epsilon|/dt = 0.0004$. The bar strength increases by 3.1% each rotation period reaching a final value of $|\epsilon| = 0.17$. As was true for the strong bar shown in Figure 12, the R1 ring weakens as the simulation progresses.

Figure 16 shows the last frame of simulation 1 and 25-29 that have different rates of change in the bar strength
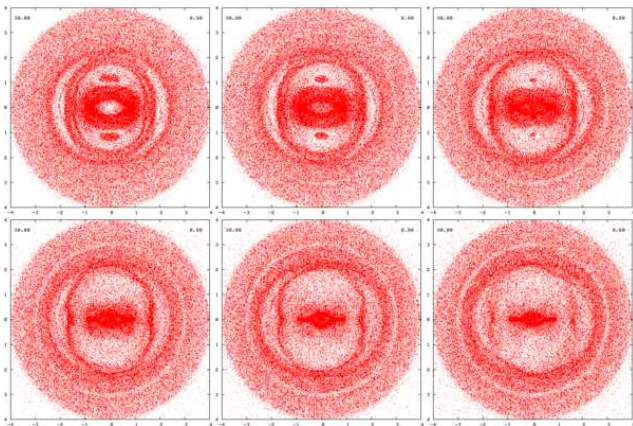
Figure 14. The last frame of the simulations in which the strength of the bar, $|\epsilon_{tgrow}|$, is varied. Each frame shows the density distribution at a time 25 bar periods after the start of the simulation. This figure shows the same simulations as Figure 13. From right to left the top row shows simulation 20 with $|\epsilon_{tgrow}| = 0.06$, simulation 21 with $|\epsilon_{tgrow}| = 0.08$ and simulation 1 with $|\epsilon_{tgrow}| = 0.10$. The bottom row shows simulation 22 with $|\epsilon_{tgrow}| = 0.12$, simulation 23 with $|\epsilon_{tgrow}| = 0.14$ and simulation 24 with $|\epsilon_{tgrow}| = 0.16$. We find that R1 rings dissolve at later times when the bar strength $|\epsilon| > 0.15$.

Figure 15. Simulation 26 showing a bar with strength increasing after bar growth, $d|\epsilon|/dt = 0.0004$. Each frame is separated by one full initial bar rotation period. As was true for the strong bar shown in Figure 12, increasing bar strength causes the R1 ring to weaken and dissolve.

following bar growth. We find that by the twenty-fifth bar period, the density distributions of these simulations exhibit the same loss of the R1 ring as the simulations in which we increased the value of the bar strength $|\epsilon_{tgrow}|$.

We can conclude that an increase in bar strength dissolves the R1 ring. We lose the R1 ring if the bar becomes 60% stronger ($|\epsilon_{tgrow}| = 0.16$ as opposed to $|\epsilon_{tgrow}| = 0.10$) or if the bar strength increases by $\sim 140\%$ compared to its initial value. It does not appear to matter whether this increase in bar strength occurs during bar growth or more slowly after bar growth is completed; we find that the R1 ring dissolves in both cases. Thus, the R1 ring dissolves for bars with higher strengths.

We now consider simulations 30-34 in which the bar strength decreases after bar growth. Figure 17 shows simulation 32 with $d|\epsilon|/dt = -0.0003$, while Figure 18 shows the last frame of simulations 1 and 30-34.

In Figure 17 showing a bar that decreases in strength after growth, we see the strong open spiral structure during and immediately following bar growth displayed by many of our simulations. The R2 ring is misaligned with the bar for ~ 5 bar periods after bar growth. After the R1 and R2 rings form, they begin to lose their respective alignments (perpendicular and parallel) with the bar in favor of more circular orientations. As shown in Figure 18, we find that the outer rings become circular at later times when the bar strength is decreased after bar growth. The simulations with the weakest bars at the end of the simulation leave behind two circular rings. NGC 2273 an unusual double-outer ring galaxy (Buta & Combes 1996), may be an example of a bar that has weakened.
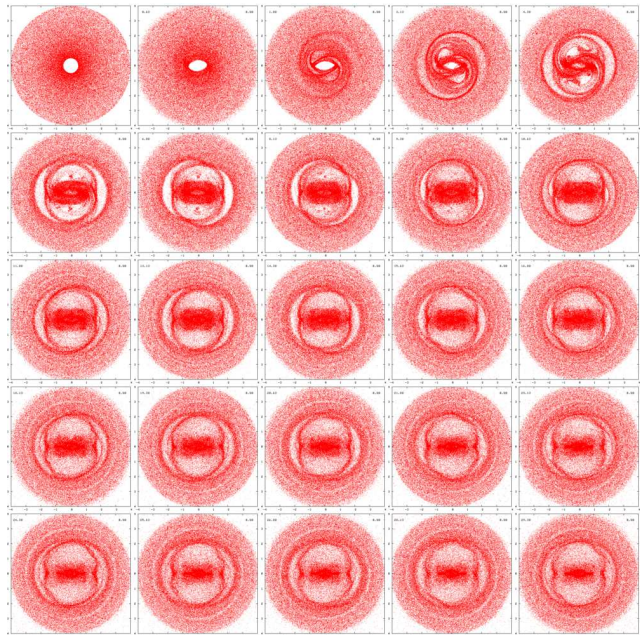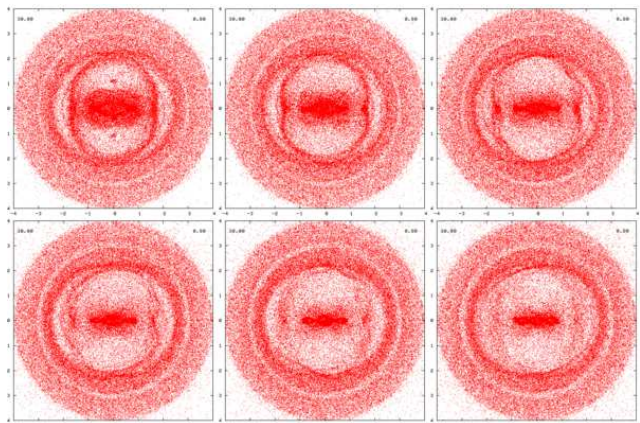

Figure 16. The last frame of each of the simulations in bar strength is increasing after $t = t_{grow}$. Each frame shows the density distribution at a time 25 bar periods after the start of the simulation. From right to left the top row shows simulation 1 with $d|\epsilon|/dt = 0.0$, simulation 25 with $d|\epsilon|/dt = 0.0002$ and simulation 26 with $d|\epsilon|/dt = 0.0004$. The bottom row shows simulation 27 with $d|\epsilon|/dt = 0.0006$, simulation 28 with $d|\epsilon|/dt = 0.0008$ and simulation 29 with $d|\epsilon|/dt = 0.0010$. We see the same loss of the R1 ring as that in Figure 14 (showing the morphology at later times as a function of bar strength) suggesting that bars with $|\epsilon| \gtrsim 0.16$ cannot maintain stable R1 rings.

2.6 Morphology sensitivity to the ratio of bar length to corotation radius

Finally, we explore the effect of altering the ratio of bar length to corotation radius. Rautiainen et al. (2008) finds that late galaxies have smaller ratios of bar length to corotation ratios, R, and weaker bars. Athanassoula (1992) and
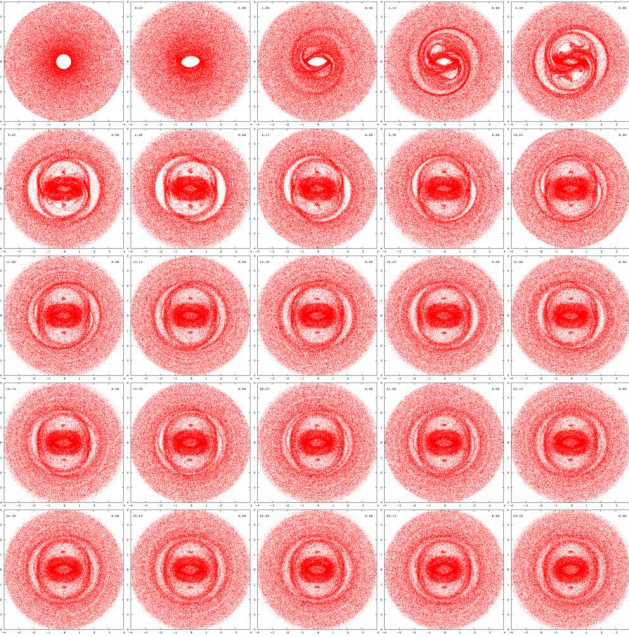
Figure 17. Simulation 32 showing a bar with decreasing strength, $d|\epsilon|/dt = -0.0003$. The bar strength decreases linearly with time after bar growth is complete. Each frame is separated by one full initial bar period. The R1 and R2 rings become more circular as the bar weakens.
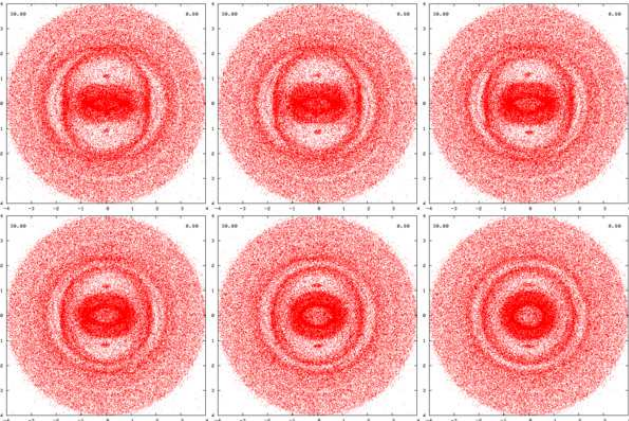

Figure 18. The last frame of each of the simulations in which the bar is decreasing in strength after growth. Each frame shows the density distribution at a time 25 bar periods after the start of the simulation. From left to right the top row shows simulation 1 with $d|\epsilon|/dt = 0.0$, simulation 30 with $d|\epsilon|/dt = -0.0001$ and simulation 31 with $d|\epsilon|/dt = -0.0002$. The bottom row shows simulation 32 with $d|\epsilon|/dt = -0.0003$, simulation 33 with $d|\epsilon|/dt = -0.0004$ and simulation 34 with $d|\epsilon|/dt = -0.0005$. As the bar becomes weaker the rings separate and become more circular. Two circular rings are left at the end of the simulations that have the weakest bars at the end of the simulation. NGC 2273 with an unusual double outer ring (Buta & Combes 1996) may be an example of a galaxy with a bar that has weakened.

Rautiainen et al. (2008) find that $R = 0.7 - 0.9$ for most galaxies. Previously we have only investigated simulations with an initial bar pattern speed of $\Omega_{b,0} = 0.8$, a corotation radius of $r_{CR} = 1.25$, and a ratio of bar length to corotation radius of $R = 0.8$. Figure 19 shows simulation 35 with an initial bar pattern speed of $\Omega_{b,0} = 0.7$. The ratio of corotation radius to bar length here is $r_{CR} = 1.43$ and the ratio of bar length to corotation radius is $R = 0.7$. Figure 20 shows simulation 36 with an initial bar patter speed of $\Omega_{b,0} = 0.9$, and $R = 0.9$. Both of these figures may be compared with simulation 1 shown in Figure 2, for which $\Omega_{b,0} = 0.8$, $r_{CR} = 1.25$ and $R = 0.8$.

In Figure 19 we note that the spiral-like structure at the end of bar growth is not as strong here as it is in Figures 2 and 20. As was true for the simulations with decreasing bar pattern speed following bar growth (see Figure 10), transient spiral structure during bar growth is weaker at slower pattern speeds. R1 and R2 rings are present 1 to 2 periods later than in Figure 2 and 2 to 3 periods later than in Figure 20. Azimuthal variations in density in the rings and shifts in the R2 ring orientation are present for up to 6 bar periods following bar growth, whereas they are present for only 5 periods in Figure 2. In Figure 20 these variations are only present up to the 4th bar period following bar growth, and the R2 ring is oriented parallel to the bar at this point. The timescale for R2 orientation changes is likely to depend on the libration timescale in the OLR. When the pattern speed is decreased with respect to the bar length, the OLR is further from the end of the bar and so is likely to have a longer libration timescale accounting for the increase in the length of time of R2 ring misalignment seen in simulation 35 (shown in Figure 19).

The rings of Figure 19 have noticeably larger radii than the rings of Figure 20. The radii of the rings shrinks as the corotation radius and the radii of the Lindblad resonances is decreased. Finally, there is a large concentration of particles in the L4 and L5 Lagrange points in Figure 19, while Figure 2 shows only a small concentration of particles corotating with the bar at the L4 and L5 points. Figure 20 shows no such concentrations in the Lagrange points. As mentioned previously, an increase in pattern speed and variations in bar strength will reduce the number of particles that are confined to these points.

3 COMPARISON TO RING GALAXY MORPHOLOGY

3.1 Sample

Following the lead of Rautiainen et al. (2008) we compare our simulations to B-band galactic images from OSUBSGS. We initially considered all galaxies in the OSUBSGS that are classified as ring galaxies, however we then restricted our choices of galaxies to those that have clearly visible outer rings in the B band images and with inclinations below $60°$, so that they could be compared to the morphology of our simulations. We also restricted our comparison galaxies to early type barred spiral galaxies as they contain less gas and dust compared to later type galaxies and so would be more appropriately compared to our collisionless dissipationless simulations. We include two additional galaxies,
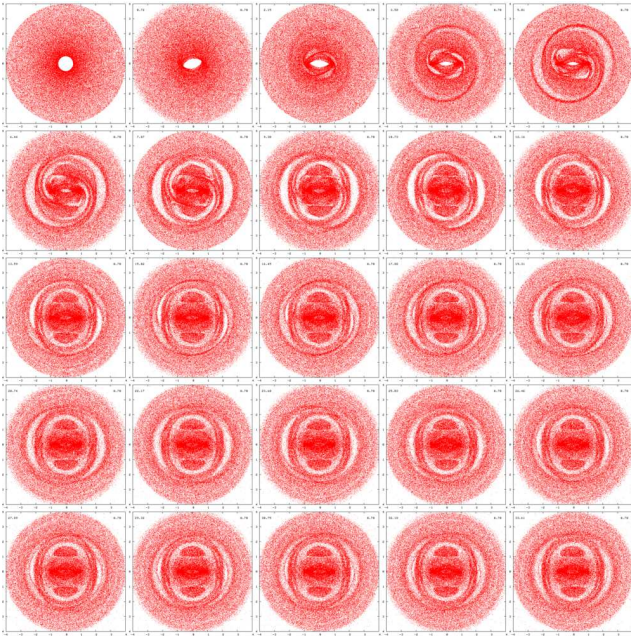
Figure 19. Simulation 35 with a slower initial pattern speed of $\Omega_{b,0} = 0.7$. The ratio of bar length to corotation radius is $R = 0.7$. Frames are separated by one full initial bar rotation period. A smaller ratio of bar length to corotation radius results in weaker spiral structure during bar growth. The R2 ring takes longer to become aligned with the bar, and the radii of the rings is larger as the resonances have moved outward.
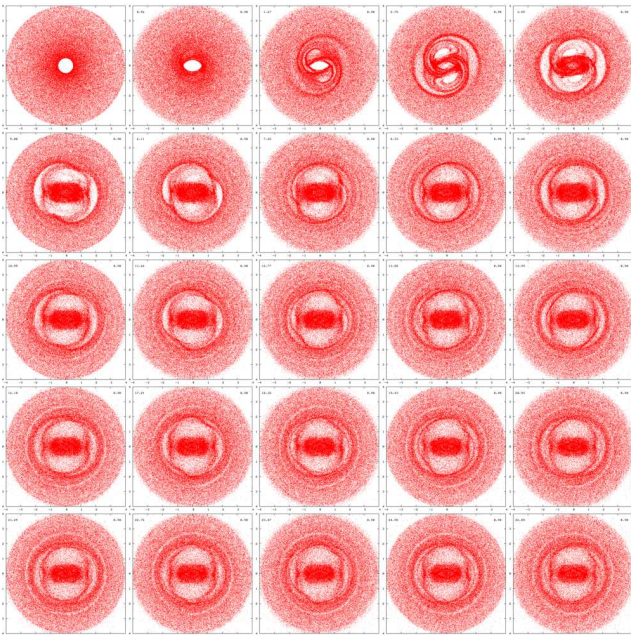

Figure 20. Simulation 36 with an initial pattern speed of $\Omega_{b,0} = 0.9$ and $R = 0.9$. Frames are separated by one full initial bar rotation period. We see stronger spiral structure during bar growth, and the R1 and R2 rings form and align (perpendicular and parallel, respectively) with the bar earlier than in simulations with slower pattern speeds. The resonances have moved inward, creating rings with smaller radii.

NGC 4314 and NGC 4548, that are not classified as ring galaxies, but have strong bars and display R1' type ring morphology. Our sample of comparison objects consists of 9 spiral galaxies with morphological classifications ranging from SB0/a to SBbc. These classifications are based on those put forth by de Vaucouleurs et al. (1976). One of the galaxies is weakly barred, NGC 4457, with maximum $Q_T \sim 0.1$ (Laurikainen et al. 2004). The galaxies that we compare to our simulations are listed in Table 3 with Hubble type, inclination with respect to the line of sight, distance, H band magnitude from the 2MASS extended source catalog, estimated circular velocity, bar length, strength and estimated bar rotation periods. Bar lengths and strengths (Q_T) are taken from the measurements by Laurikainen et al. (2004). Distances in Mpc from the HyperLeda database (Paturel et al. 2003) calculated using velocities corrected for infall of the Local Group towards Virgo and a Hubble constant $H_0 = 70$ km s^{-1} Mpc $^{-1}$. Inclinations are those from the HyperLeda database (Paturel et al. 2003). The circular velocity is estimated from the H band magnitude and the luminosity line width relation by Pierce & Tully (1992).

For each galaxy in our comparison sample we ran simulations with bar strengths that matched those measured by Laurikainen et al. (2004). When comparing galaxies to our simulations, we focus on the location, orientation and morphology of the spiral arms and outer rings. We searched through our bank of simulations for images that best resembled the outer ring galaxy morphology. Galaxy images have been corrected for inclination and rotated so that the bar lies horizontal in our figures. In some cases the galaxy images have been flipped so that the galaxy is rotating counter clockwise and so is in the same direction as our simulations.

We first compare galaxies with strong R1' pseudoring morphology to morphology displayed by our simulations during bar growth. We then focus on galaxies with R1R2 rings. Finally we explore simulations that can account for the weak bar and distant outer ring present in NGC 4457.

3.2 Comparison of particle simulations to galaxies exhibiting similar spiral-like structure

Figure 21 shows four galaxies, with strong R1' type pseudorings; NGCs 4548, 7552, 1300, and 4134. To best match their pseudoring morphology, we chose simulations with $\Omega_{b,0} = 0.8$ and a bar that grows in three bar periods. Each of the galaxy images is compared with the density distribution at a time during or just following bar growth. NGC 4548 and NGC 7552 have the weakest strengths $Q_T = 0.34$ and 0.4 respectively. NGC 4314 and NGC 1300 have stronger bars with $Q_T = 0.44$ and 0.54 respectively. The simulations show stronger spiral structure at late times during bar growth and for stronger bars. Thus we chose a relatively early time (1.5 bar periods since the beginning of the simulation) for the simulation matching NGC 4548 which has weaker spiral structure and later times for the other galaxies ($t = 2P_{b,0}$, $2.5P_{b,0}$ and $4P_{b,0}$ for NGC 7552, NGC 1300 and NGC 4314, respectively). NGC 1300 has the strongest spiral structure but also has the strongest bar. A later time in the simulation is required to match the NGC 1300's longer spiral arms. NGC 4314's spiral structure is not as narrow as for the other galaxies. We find a better match of morphologies between NGC 4314 and our simulation when we increase the initial

velocity dispersion of our simulation from 0.04 to 0.07. The outer disk of NGC 4314 is devoid of star formation suggesting that an initial velocity dispersion typical of a stellar disk rather than a gaseous one should be used. The increase in velocity dispersion decreases the strength of the arms displayed by the simulation, requiring a later time to match the observed morphology.

We find that our simulations display reasonable matches to observed R1' ring morphology near the end of bar growth when strong spiral pseudorings are displayed by our simulations. It is likely that these galaxies have experienced recent bar growth. These bars could still be growing. We note that R1' pseudoring structure is displayed for a longer timescale (up to a few bar rotation periods following bar growth) by SPH and sticky particle simulations (Byrd et al. 1994; Ann & Lee 2000). This comparison suggests that our dissipationless simulations could underestimate the longevity of R1' structure.

3.3 R1R2 rings

We now compare our simulations to galaxies that display R1R2 morphology which is exhibited by our simulations following bar growth. We begin by comparing our simulations to two galaxies that exhibit R1R2' morphology. Depending on the strength of the bar, the R2 ring can remain misaligned with the bar for up to ~ 10 bar periods following growth. Figure 22 shows R1R2' galaxies that exhibit structure similar to that in our simulations that is evident before the R2 ring aligns with the bar. From top to bottom Figure 22 shows NGC 5701, and NGC 5101.

Figure 23 compares NGC 6782 and NGC 3504 with density distributions showing simulations that have stabilized and exhibit R1R2 morphology.

NGC 5701 is a fairly weak bar with $Q_T = 0.14$ that shows a strong R1 ring but a weaker R2 ring. NGC 5701 is compared to a simulation one period after bar growth has completed. At this time the spiral arms generated during bar growth are beginning to close and will soon form both R1 and R2 rings. As NGC 5701 has a weaker bar it may take longer for R1 and R2 rings to form and become aligned perpendicular and parallel with the bar, respectively.

NGC 5101 is somewhat stronger with $Q_T = 0.19$, and displays both R1 and R2 rings. It is compared to a simulation 7.5 periods following bar growth. The R2 ring at this time is misaligned with the bar similar to the misalignment in the galaxy. The galaxy displays a more elliptical ring than that of our simulation. A number of factors could account for this discrepancy. The bar could be slowing down and causing increased epicyclic motion in the R2 ring due to resonance capture. We may not have corrected for inclination correctly, or the rotation curve could be dropping in this region, causing the OLR to be stronger than we have considered here with a flat rotation curve.

The simulations we have chosen to match the galaxies with R1R2 morphology have bars with fixed pattern speeds. Reasonable matches between observed and simulated morphology are found a few periods following bar growth during which time our simulations contain both R1 and R2 rings but still exhibit asymmetries in the R2 ring. Based on the exploration in section 2.2 we can conclude that the bars in these galaxies are unlikely to have increased in pattern
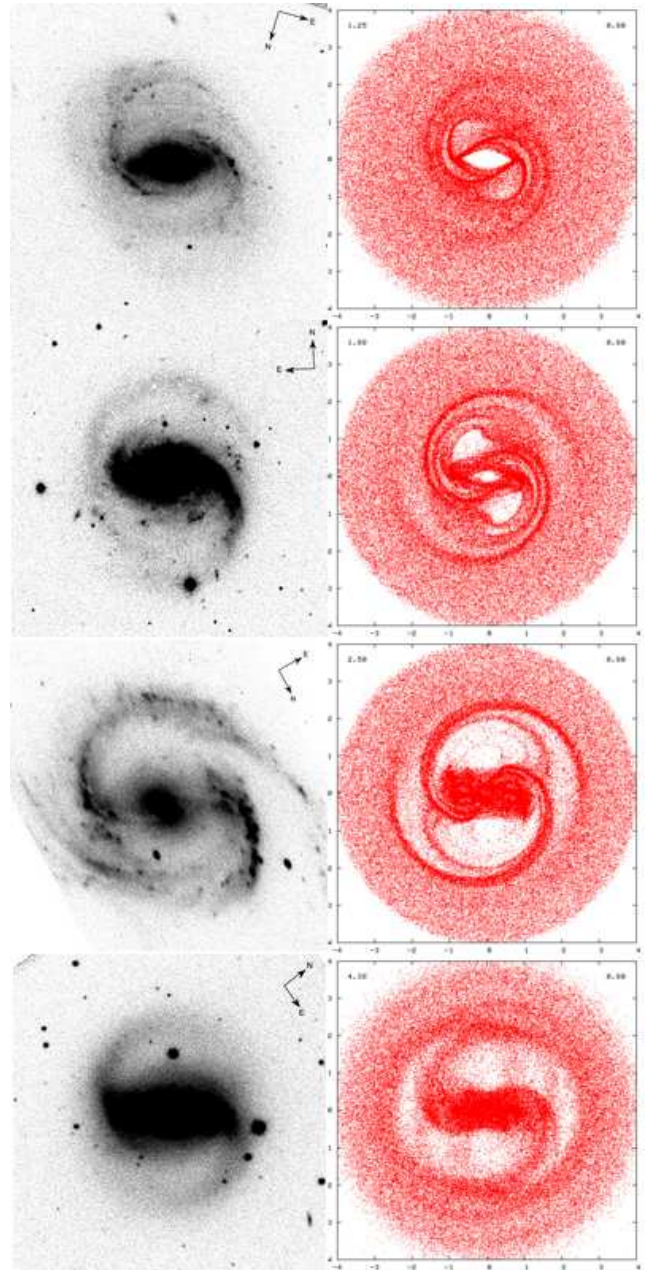

Figure 21. We compare the pseudorings of four galaxies with the structure created during bar growth in our simulations. From top to bottom, Row 1 shows NGC 4548 with $Q_T = 0.34$, Row 2 NGC 7552 with $Q_T = 0.4$, Row 3 NGC 1300 with $Q_T = 0.54$, and Row 4 shows NGC 4314 with $Q_T = 0.44$. Galaxy images are on the left and simulations on the right. Galaxy images have been corrected for inclination and rotated so that the bar lies horizontal. In some galaxies the galaxy image has been inverted so that the galaxy is viewed rotating counter clockwise. The simulation for NGC 4548 is shown at $t = 1.5P_{b,0}$, (for $P_{b,0}$ initial bar rotation periods) from the beginning of the simulation. That for 7552 is shown at $t = 2P_{b,0}$, that for NGC 1300 at $t = 2.5P_{b,0}$ and that for NGC 4314 at $4P_{b,0}$. The simulation for NGCs 4548, 7552 and 1300 are shown during bar growth, and that for NGC 4314 1 period after bar growth. The initial orbits for the NGC 4314 simulation had twice the velocity dispersion of the other simulations.
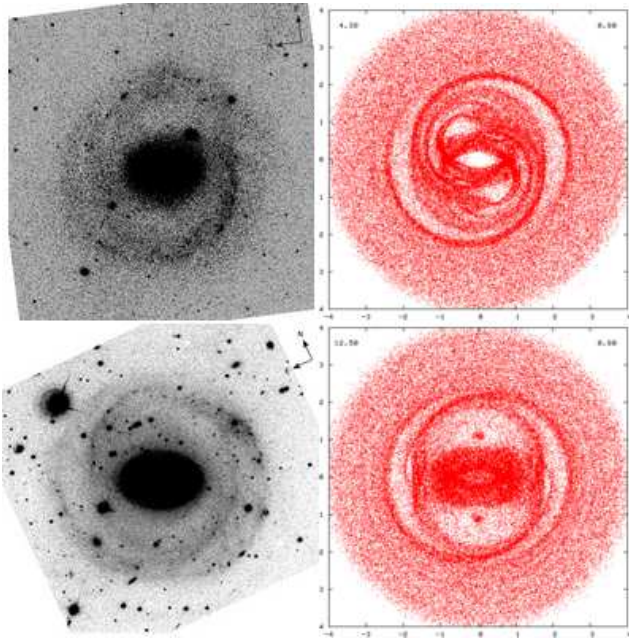
Figure 22. The top row shows NGC 5701, $Q_T = 0.14$, compared with the 4th period of a simulation with a bar of strength $|\epsilon_{tgrow}| = 0.07$ 1 period after bar formation. The bottom row shows NGC 5101, $Q_T = 0.19$, compared with the density distribution of a simulation with a bar of strength $|\epsilon_{tgrow}| = 0.095$ 7.5 periods after bar formation. The ring structure of these galaxies is similar to the broken or misaligned rings shown in our simulations a few rotation periods following bar growth.

Figure 23. We compare NGC 6782 and NGC 3504 to density distributions of simulations 2 periods after bar growth. The top row compares NGC 6782, $Q_T = 0.17$, to a simulation with a bar of strength $|\epsilon_{tgrow}| = 0.085$. The bottom row shows NGC 3504, $Q_T = 0.29$, compared to a simulation with $|\epsilon_{tgrow}| = 0.145$. The bars of these galaxies may be responsible for the R1 structure visible in these images. The galaxies' R2 rings may be present but not visible in the B-band.

speed as this would have destroyed the R1 ring. Moderate decreases in bar pattern speed could have occurred.

We now compare our simulations to two galaxies that exhibit R1R2 morphology. In Figure 23 NGC 6782 and NGC 3504 are both compared to the eleventh frame of simulations with bars of strengths $|\epsilon_{tgrow}| = 0.085$ and 0.145, respectively. Both simulations are shown 2 periods after bar growth.

NGC 6782 is an (R')SB(r)0/a galaxy with an inclination of $56.0°$ and $Q_T = 0.17$. Because of the weaker bar, the R2 ring in NGC 6782's comparison simulation remains misaligned with the bar for ~ 6 bar periods following bar growth. The spiral-like structure evident during bar growth does not close to form R1 and R2 rings until 2 periods after bar growth, in the frame shown in Figure 23. There is a reasonable match between the R1 structure of NGC 6782 and that exhibited by our simulation.

NGC 3504 is classified as an (R)SAB(s)ab galaxy with an inclination of $53.4°$ and $Q_T = 0.29$. NGC 3504 has a much stronger bar than NGC 6782. R1 and R2 rings are evident only 1 period after bar growth, and the R2 ring is aligned with the bar within 4 bar rotation periods following bar growth. As with NGC 4314 in Figure 22, the strong bar leads to a weakening of the R1 ring.

Sticky particles simulations by Schwarz (1984) displayed R1 or R2 morphology depending on the initial gas distribution. Either dissipation is required to exhibit R1 morphology only, or the initial stellar and gas distribution is different for the galaxies showing longer lived R1 morphology.
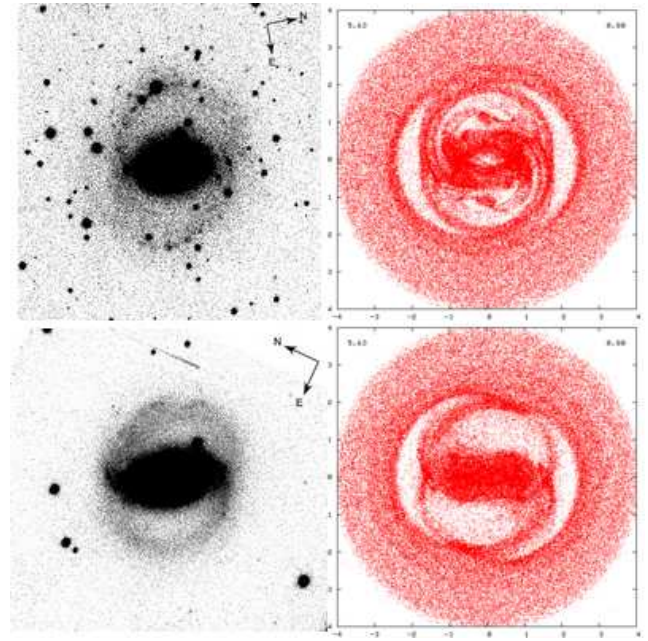
3.4 Dissolving the R1 ring and NGC 4457

We found in section 2.2 that the R1 ring dissolves when the bar pattern speed increases by more than $\sim 8\%$ after bar growth. We see the same loss of the R1 ring if the bar has strength $|\epsilon_{tgrow}| > 1.5$ or if the bar strength increases by $\gtrsim 140\%$ after bar growth. In either case, the R1 ring is destroyed leaving a nearly circular R2 ring.

NGC 4457, an (r)SAB(s)0/a galaxy, appears to be lacking an R1 ring. According to Laurikainen et al. (2004) NGC 4457's bar has $Q_T = 0.09$, which corresponds to a very weak bar. It is therefore unlikely that loss of the R1 ring is due to the strength of the bar, as we find that strong bars dissolve the R1 ring and weakening bars can leave behind a double ring. It is possible, however, that the lack of an R1 ring is the result of a bar that has increased in pattern speed. For this reason, in Figure 24 we compare NGC 4457 with the last frame ($t = 25P_{b,0}$) of simulation 5, which has a bar that is speeding up after bar growth, $d\Omega_b/dt = 0.0004$. NGC 4457's outer rings are very faint in the B-band image, yet it does appear that the outer ring is circular and no R1 ring is evident. It is possible that the pattern speed of this galaxy's bar has increased since the bar finished growing, thereby destroying any R1 ring that would have formed shortly after bar growth.

4 DISCUSSION AND SUMMARY

We have presented integrations of collisionless massless particles perturbed by growing and secularly evolving bar per-
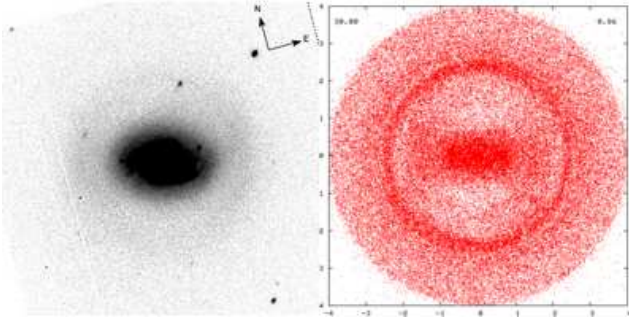
Figure 24. NGC 4457 compared to the 25th frame of simulation 5, which has a bar with increasing pattern speed; $d\Omega_b/dt = 0.0004$. Both the galaxy and the simulation lack an R1 outer ring but do maintain a nearly circular outer ring.

turbations. We find that collisionless simulations can exhibit double ringed R1 and R2 outer ring morphology with rings both perpendicular (R1) and parallel (R2) to the bar. In the last period of bar growth, strong open spiral structure is exhibited resembling an R1' pseudoring. For 2-3 periods following bar growth R1 and R2 rings are seen with the R2 ring changing in orientation and azimuthal density contrast. Thus R1R2' pseudoring morphology is displayed within a few bar periods following bar growth. Our simulations start with particles in nearly circular orbits with velocity dispersions equivalent to 7 km/s for a 200 km/s rotation curve. This suggests sticky particle simulations have been successful in exhibiting R1R2 ring morphology because the velocity dispersion of orbits is damped and so particles are in initially nearly circular orbits.

In our collisionless simulations we find that the outer rings with major axis perpendicular (R1) to the bar are fragile. If the bar pattern speed increases more than 8% after bar growth, or if the bar strength is higher than or increases past $|\epsilon| \gtrsim 0.16$ or $Q_T \gtrsim 0.32$ the R1 outer ring will dissolve after ~ 20 twenty bar periods. The simulations are then nearly mirror symmetric and do not display asymmetries typical of pseudorings.

Stronger bars can form R1' pseudorings earlier. However if the bar strength $|\epsilon| \gtrsim 0.16$ or $Q_T \gtrsim 0.32$ the R1 ring will dissolve after ~ 20 bar rotation periods. If the bar strength increases to this value subsequent to formation, the R1 ring also dissolves.

We find that a decrease in the bar pattern speed after bar growth causes particles to be captured in orbits parallel to the bar which are increased in epicyclic amplitude as the bar slows down. Strong R1 and elongated R2 rings persist in these simulations. Misalignments between the R2 ring and the bar also persist so the galaxy can exhibit R1R2' pseudoring morphology for a longer period of time. If the bar pattern speed slows down more than $\sim 3.5\%$ the R2 ring develops a scallop above and below the bar. As these are not observed in galaxies, bars probably do not slow down more than $\sim 3.5\%$ without also varying in strength.

Sandage & Bedke (1994) find that early type barred galaxies often have semi-detached outer rings (e.g, NGC 1543, Buta & Combes 1996 and NGC 4457). These galaxies may contain bars that have increased in pattern speed or were once strong and so destroyed their R1 ring. If the bar weakens the R1 and R2 rings can be left behind as two

nearly circular rings, similar to those observed in the unusual double outer ringed galaxy NGC 2273.

We find that the morphology of our simulations resembles that of R1' ringed galaxies if the simulation time is chosen during or just after bar formation. We find we can match pseudoring morphology with simulations that have bar strengths estimated from the bar shapes. Stronger and longer spiral arms are seen later in the simulation and in more strongly barred systems. The constraint on simulation timescale suggests that R1' ring morphology is a signpost of recent bar formation. We note that sticky particle and SPH simulations exhibit R1 pseudoring morphology a few bar rotation periods longer than ours suggesting that the dissipationless simulations explored here underestimate the longevity of these features.

We find that galaxies with R1R2' morphology are well matched by simulations a few bar rotation periods following bar growth. As R1 rings are fragile, we infer that these galaxies have had stable bars that have not experienced large changes in either pattern speed or strength.

The exploration of parameter space in the collisionless dissipationless limit done here can be used by future work to differentiate between phenomena that would be exhibited by collisionless models and that that is a result of dissipation. A better understanding of the role of dissipation in affecting outer ring morphology should allow observationally based constraints on the secular evolution of bars.

Only 10-20% of early type galaxies exhibit outer rings with pseudorings being more prevalent in later type galaxies (Buta & Combes 1996). Not all but most galaxies classified with outer rings are barred suggesting that only 15-40% of barred galaxies exhibit outer rings. Here we have found that R1' and R1R2' galaxies are likely to represent different times since bar formation with R1' galaxies representing an earlier timescale during or just after bar formation and R1R2 morphology representing galaxies with stable bars a few bar rotation periods following bar formation. Galaxies in these two transient categories probably comprise a significant fraction of all outer ring galaxies. This suggests that most outer ring galaxies represent morphology that is only present for a few bar rotation periods. It is interesting to ask what timescales these morphologies correspond to. Bar rotation periods for the ringed galaxies in our sample range from $\sim 100 - 200$ Myr (see 3). The R1' classification, may only last a few bar rotations or 1/2 Gyr and the R1R2' classification only ~ 1 Gyr. Both of these timescales are short compared to the lifetime of a galaxy. Ringed galaxies lacking R1 rings may be longer lived but may provide evidence for bar evolution. It is likely that only a low fraction of barred galaxies might be considered systems that are not evolving secularly or have not formed in the last Gyr.

5 ACKNOWLEDGMENTS

REFERENCES

Ann, H. B., & Lee, H. M. 2000, JKAS, 33, 1

Athanassoula E. 1992, MNRAS, 259, 345

Athanassoula, E. 2003, MNRAS, 341, 1179

Bissantz, N., Englmaier, P., & Gerhard, O. 2003, MNRAS, 340, 949

Bournaud, F., & Combes, F. 2002, A&A, 392, 83

Buta, R., & Combes, F. 1996, Fund. Cosmic Physics, 17, 95

Byrd, G., Rautiainen, P., Salo, H., Buta, R., & Crocker, D. A. 1994, AJ, 108, 476

Combes, F., & Sanders, R. H. 1981, A&A, 96, 164

Combes, F., & Gerin, M. 1985, A&A, 150, 327

Contopoulos, G. & Grosbol, P. 1989, Astr. Astrophys. Rev., 1, 261.

Contopoulos, G. & Patsis, P. A. 2006, MNRAS¡ 369, 1054

Das, M., Teuben, P. J., Vogel, S. N., Regan, M. W., Sheth, K., Harris, A. I., & Jefferys, W. H. 2003, ApJ, 582, 190

Debattista, V. P., & Sellwood, J. A. 1998, ApJ, 493, L5

Dehnen, W. 2000, AJ, 119, 800

de Vaucouleurs G., de Vaucouleurs A., & Corwin, H. G., 1976, Second Reference Catalogue of Bright Galaxies, University of Texas Press, Austin London

de Vaucouleurs G., de Vaucouleurs A., Corwin H. G., Jr, Buta R., Paturel G., Fouque P., 1991, Third Reference Catalogue of Bright Galaxies. Springer-Verlag, New York

Eskridge, P. B., Frogel, J. A., Pogge, R. W., Quillen, A. C., Berlind, A. A., Davies, R. L., DePoy, D. L., Gilbert, K. M., Houdashelt, M. L., Kuchinski, L. E., Ramírez S. V., Sellgren, K., Stutx, A., Terndrup, D. M., Tiede, G. P., 2002, ApJS, 143, 73

Gadotti, D. A., & de Souza, R. E. 2006, ApJS, 163, 270

Hunter, J. H., Jr., England, M. N., Gottesman, S. T., Ball, R., & Huntley, J. M. 1988, ApJ, 324, 721

Jarrett, T. H., Chester, T., Cutri, R., Schneider, S., Skrutskie, M., Huchra, J. P. 2000, AJ, 119, 298

Kalnajs, A. J. 1991, in Dynamics of Disc Galaxies, ed. B. Sundelis, Göteborg, Sweden, p. 323

Laurikainen, E., Salo, H., Buta, R., & Vasylyev, S. 2004, MNRAS, 355, 1251

Lindblad, P. A. B., Lindblad, P. O., & Athanassoula, E. 1996, A&A, 313, 65

Martinez-Valpuesta, I., Shlosman, I., & Heller, C. 2006, ApJ, 637, 214

Minchev, I., Nordhaus, J., & Quillen, A. C. 2007, ApJ, 664, L31

Paturel, G., Petit, C., Prugniel, P., Theureau, G., Rousseau, J., Brouty, M., Dubois, P., & Cambrésy, L. 2003, A&A, 412, 45

Pierce, M. J. & Tully, R. B. 1992, ApJ, 387, 47

Quillen, A. C. 2003, AJ, 125, 785

Quillen, A C., 2006, MNRAS, 365, 1367

Rautiainen, P., Salo, H., & Laurikainen, E. 2008, MNRAS, in press, arXiv0806.0471

Rautiainen, P., Salo, H., & Buta, R. 2004, MNRAS, 349, 933

Rautiainen, P., & Salo, H. 2000, A&A, 362, 465

Romero-Gomez, M., Masdemont, J. J., Athanassoula, E., & Garcia-Gomez, C. 2006, AA, 453, 39

Salo, H., Rautiainen, P., Buta, R., Purcell, G. B., Cobb, M. L., Crocker, D. A., & Laurikainen, E. 1999, AJ, 117, 792

Sandage, A. and Bedke, J. 1994, The Carnegie Atlas of Galaxies, Carnegie Inst. of Wash. Publ. No. 638

Schwarz, M. P. 1981, ApJ, 247, 77

Schwarz, M. P. 1984, Proc. Astr. Soc. Australia, 5, 464

Sellwood, J. A., & Debattista, V. P. 2006, ApJ, 639, 868

Voglis, N., Harsoula, M., & Contopoulos, G. 2007, MNRAS, 381, 757

Table 1. Common Parameters for Simulations

	Parameter	Value	Comments
1	γ	0.0	Sets the slope of the rotation curve
2	t_{grow}	3	Bar growth time in bar rotation periods
3	$\Omega_{b,0}$	0.8	Initial bar pattern speed
4	$r_{b,0}$	1.0	Initial bar length
5	r_{CR}	1.25	Radius of corotation
6	R	0.8	Ratio of bar length to corotation radius
7	σ	0.036	Initial velocity dispersion in units of the circular velocity

With the exception of simulations 35 and 36, these parameters are not altered from simulation to simulation. Length scales are given in units of the initial bar length. Angular rotation rates are given in units of that at $r_{b,0}$. The initial bar rotation period is $P_{b,0} = 2\pi/\Omega_{b,0}$. For simulation 35, $\Omega_{b,0} = 0.7$, $r_{CR} = 1.43$ and $R = 0.7$. For simulation 36, $\Omega_{b,0} = 0.9$, $r_{CR} = 1.1$ and $R = 0.9$.

Table 2. Additional parameters for Simulations

Sim.	$d\Omega_b/dt$	%	$d\Omega_g/dt$	%	$|\epsilon_{tgrow}|$	$d|\epsilon|/dt$	%
1	2	3	4	5	6	7	8
1	0.00	0.00	0.0	0.0	0.10	0.0	0.0
2	0.0001	2.16	0.0	0.0	0.10	0.0	0.0
3	0.0002	4.32	0.0	0.0	0.10	0.0	0.0
4	0.0003	6.48	0.0	0.0	0.10	0.0	0.0
5	0.0004	8.64	0.0	0.0	0.10	0.0	0.0
6	0.0005	10.80	0.0	0.0	0.10	0.0	0.0
7	-0.0001	-2.16	0.0	0.0	0.10	0.0	0.0
8	-0.00015	-3.24	0.0	0.0	0.10	0.0	0.0
9	-0.0002	-4.32	0.0	0.0	0.10	0.0	0.0
10	-0.00025	-5.40	0.0	0.0	0.10	0.0	0.0
11	-0.0003	-6.48	0.0	0.0	0.10	0.0	0.0
12	0.0	0.0	0.005	14.73	0.10	0.0	0.0
13	0.0	0.0	0.01	29.45	0.10	0.0	0.0
14	0.0	0.0	0.015	44.18	0.10	0.0	0.0
15	0.0	0.0	0.02	58.90	0.10	0.0	0.0
16	0.0	0.0	-0.0025	-7.36	0.10	0.0	0.0
17	0.0	0.0	-0.005	-14.73	0.10	0.0	0.0
18	0.0	0.0	-0.0075	-22.09	0.10	0.0	0.0
19	0.0	0.0	-0.01	-29.45	0.10	0.0	0.0
20	0.0	0.0	0.0	0.0	0.06	0.0	0.0
21	0.0	0.0	0.0	0.0	0.08	0.0	0.0
22	0.0	0.0	0.0	0.0	0.12	0.0	0.0
23	0.0	0.0	0.0	0.0	0.14	0.0	0.0
24	0.0	0.0	0.0	0.0	0.16	0.0	0.0
25	0.0	0.0	0.0	0.0	0.10	0.0002	34.56
26	0.0	0.0	0.0	0.0	0.10	0.0004	69.12
27	0.0	0.0	0.0	0.0	0.10	0.0006	103.7
28	0.0	0.0	0.0	0.0	0.10	0.0008	138.2
29	0.0	0.0	0.0	0.0	0.10	0.0010	172.8
30	0.0	0.0	0.0	0.0	0.10	-0.0001	-17.28
31	0.0	0.0	0.0	0.0	0.10	-0.0002	-34.56
32	0.0	0.0	0.0	0.0	0.10	-0.0003	-51.84
33	0.0	0.0	0.0	0.0	0.10	-0.0004	-69.12
34	0.0	0.0	0.0	0.0	0.10	-0.0005	-86.39
35	0.0	0.0	0.0	0.0	0.10	0.0	0.0
36	0.0	0.0	0.0	0.0	0.10	0.0	0.0

Length-scales are given in units of the initial bar length. Velocities are given in units of the circular velocity at the initial bar end. Time is given in units such that the period of rotation is 2π at $r_{b,0}$. Angular rotation rates are in units of that at $r_{b,0}$. The initial bar period $P_{b,0} = 2\pi/\Omega_{b,0}$. Bar strength is given in units of the square of the circular velocity at $r_{b,0}$. By Column Col. (1): Simulation. Col. (2): $d\Omega_b/dt$ is the rate of bar pattern speed change after bar growth. Col. (3): The percent by which the bar pattern speed has changed by $t = 25P_{b,0}$, after twenty-five bar rotation periods. Col. (4): $d\Omega_g/dt$ is the rate of bar pattern speed change during bar growth. Col. (5): The percent by which the bar pattern speed has changed by the end of bar growth. Col. (6): ϵ_{tgrow} is the bar strength at the end of bar growth or at time $t = t_{grow}$. Col. (7): $d\epsilon/dt$ is the bar strength rate of change after t_{grow}. Col. (8): The percent by which the bar strength changes by $t = 25P_{b,0}$. Note: Simulations 35 and 36 have initial bar pattern speeds of $\Omega_{b,0} = 0.7$ and 0.9, respectively, whereas all other simulations have $\Omega_{b,0} = 0.8$ (see Table 1).

Table 3. Ring Galaxy Estimated Bar Rotation Periods

	Type	i	Q_T	D Mpc	m_H mag	M_H mag	v_c km/s	r_b kpc	P_b Myr
	1	2	3	4	5	6	7	8	9
NGC 1300	(R')SB(s)bc	49.3	0.54	20.1	7.770	-23.7	258.6	8.5	206.7
NGC 3504	(R)SAB(s)ab	53.4	0.29	23.9	8.609	-23.3	234.7	7.0	187.6
NGC 4314	SB(rs)a	16.2	0.44	16.4	7.725	-23.3	234.7	6.0	160.7
NGC 4457	(R)SAB(s)0/a	34.6	0.09	13.4	8.015	-22.6	198.1	2.9	92.0
NGC 4548	SB(rs)b	37.0	0.34	8.5	7.373	-22.3	184.2	2.8	95.5
NGC 5101	(R)SB(rs)0/a	23.2	0.19	25.2	7.401	-24.6	321.7	8.5	166.2
NGC 5701	(R)SB(rs)0/a	41.3	0.14	22.9	8.358	-23.4	240.5	5.5	143.8
NGC 6782	(R')SB(r)0/a	56.0	0.17	52.0	9.115	-24.5	314.0	11.7	234.4
NGC 7552	(R')SB(s)ab	23.6	0.40	20.1	7.840	-23.7	258.6	6.8	165.3

By Column Col. (1): Morphological classifications by de Vaucouleurs et al. (1976), except those for NGC 1300 and NGC 6782, which are by de Vaucouleurs et al. (1991). Col. (2): Inclinations from the HyperLeda database (Paturel et al. 2003). Col. (3): Maximum gravitational bar torque per unit mass per unit square of the circular speed measured by Laurikainen et al. (2004). Col. (4): Distances in Mpc from the HyperLeda database (Paturel et al. 2003) calculated using velocities corrected for infall of the Local Group towards Virgo and a Hubble constant $H_0 = 70$ km s^{-1} Mpc $^{-1}$. Col. (5): Total integrated flux magnitudes in H band from the 2MASS extended source catalog (Jarrett et al. 2000). Col. (6): Absolute magnitudes in the H band. Col. (7): Circular velocities estimated from the H-band magnitude using the luminosity line widths relation by Pierce & Tully (1992). Col. (8): Bar lengths measured by Laurikainen et al. (2004). In their paper Laurikainen et al. (2004) define the bar length to be the radius of the bar region at which the phases of the $m = 2$ and $m = 4$ density amplitudes are constant. Col. (9): Periods of bar rotation calculated using the angular frequencies defined by $\Omega = v_c/r_b$.